National University of Science and Technology Politehnica Bucharest

Doctoral School on Engineering and Applications of Lasers and Accelerators

Vlad Jan Gaciu

Machine Learning and Image Processing in Experiments with Lasers and Plasmas

Ph.D. Thesis Summary

Thesis Advisor

CS1 Dr. Cătălin M. Ticoș

Bucharest, 2026

Contents

List of Figures

List of Tables

Chapter 1

Introduction

1.1 History

Artificial Intelligence (AI) is currently an extremely popular field with frequent innovation, an abundance of applications, and is also a highly active area of research. A subset of AI is the field which specializes in extracting patterns from raw data, known as Machine Learning (ML). ML techniques include a wide variety of methods used for training machines. These techniques can be generalized into three main categories: supervised, unsupervised, and reinforcement learning. A subset of ML is known as Deep Learning (DL). DL uses multiple layers of neural networks to solve problems in classification, regression, and representation learning.

1.1.1 Machine Learning Theory

What is Machine Learning (ML)? ML is essentially data-driven computer programming. It is possible to introduce large datasets of information, and output useful results without the computer being explicitly programmed to do so. ML systems iteratively optimize a model's internal parameters against a provided objective function, and are capable of improving over time [10]. For learning to work, there are three fundamental components that structure an ML system: the model (h), the loss function (L), and the optimizer. The model is a mathematical function $h(x) = y$ that maps an input x to an output y. The loss function measures the error in the ML system. The optimizer is where the learning happens during the optimization process. The system calculates the gradient of the loss function and adjusts the model's weights to minimize the error function.

1.2 Machine Learning in Physics

ML can discover new physical laws and equations. Deep neural networks have been used to solve partial differential equations [12]. These algorithms manage to find solutions to incomplete models and incomplete data. In physics-informed machine learning, the models are trained on data while using physical equations as the loss functions. The loss function includes a physics equation and is designed to penalize the model for violating physical principles. The idea behind physics-informed machine learning is to include the known laws of physics, which improves the accuracy of the model. This approach applies deep learning techniques with fundamental domain knowledge in physics to create a more reliable model of the physical world. As an example, when trying to model fluid mechanics, the Navier-Stokes equation would be ideal in the loss function to penalize inconsistencies to real world physics.

1.3 Convolutional Neural Networks

DL has been shown to be extremely useful in many fields of physics, from astrophysics to particle physics. This success is primarily a result of both fields requiring vasts amount of data. DL can recognize patterns or trends in the data much more efficiently and accurately compared to traditional computational methods. DL for optics is a perfect fit as optics data can be represented well as visual data. This type of data is aided by convolutional filters. Convolutional layers, unlike FC layers, utilize the spatial relationship between nearby values. This type of layer uses a set of kernels or filters, for example 3x3 or 5x5 for two-dimensional image kernels. The image will be convolved with the output from the previous layer.

1.4 Machine Learning Techniques

1.4.1 Supervised Learning

Supervised learning is split into classification or regression problems. In supervised learning labeled data is used for training, and to predict labels on unseen test data accurately. The techniques which are included in supervised learning include linear regression, logistic regression, K-nearest neighbours. In linear regression we use the following formula: $y_i = \beta_0 + \beta_1 x_i + \varepsilon_i$. The model is approximating a best fit line through all the data points. The model is useful in predicting outputs considering inputs with continuous values. Logistic regression outputs a probability given discrete input values. The model for logistic regression is as follows:

$$P(y_i = 1 \mid \mathbf{x}_i) = \frac{1}{1 + \exp\big(-(\beta_0 + \mathbf{x}_i^\top \boldsymbol{\beta})\big)}$$

1.4.2 Unsupervised Learning

In unsupervised learning there are clustering techniques and autoencoder neural networks. The key component which makes a method unsupervised is not having used human labels on data. In clustering techniques the data is grouped based on similar data points and assigned a class. Classically, unsupervised learning attempts to find the ideal representation for the given task. In the case of images, data points correspond to pixels, and each pixel has 3 features represented by their RGB values. Here is the model for k-means clustering:

$$J = \sum_{i=1}^{n} \min_{1 \le j \le k} \|\mathbf{x}_i - \boldsymbol{\mu}_j\|^2$$

1.5 High Power Laser Systems

The word laser is an acronym for the mechanism by which light is produced: light amplification by stimulated emission of radiation. There are many types of lasers, but the key similarity is the gain medium. This medium is composed of material capable of becoming excited by light, and consequently producing photon emission through de-excitation. This physical principle of stimulated emission was discovered by Albert Einstein in 1916. Since this discovery it was expected that lasers would present a great scientific and technological leap forwards, even before the first construction of the laser in 1960 by T.H. Maiman. Oscillators and amplifiers have since inspired and benefited thousands of scientists and engineers. Initial jumps in peak power were recorded after the inventions of Q-switching and mode-locking.

1.5.1 Fundamental Enabling Technologies

CPA

Chirped Pulse Amplification (CPA) is a pivotal invention now used by all ultra-intense laser systems. This technology allows ultrashort optical pulses to be amplified to high peak powers without damaging optical components. This technique won the 2018 Nobel Prize in Physics, and was awarded to the founders Donna Strickland and Gerard Mourou for their 1985 introduction of this technology. CPA is now the motivation for functional petawatt-class laser systems, including the ELI-NP HPLS.

The motivation for this technology is that direct amplification of femtosecond pulses is not possible due to very high peak intensities that would destroy the optical components. PCA functions in three parts: pulse stretching, pulse amplification, and pulse compression. This method of modifying the pulse functions by first stretching the pulse in time before amplification, lowering the instantaneous power, and then recompressing the pulse to receive a pulse with its original duration. Initially, a short pulse is stretched to picoseconds or nanoseconds and then amplified, following up with pulse compression to attain a femtosecond pulse duration.

The oscillator produces a seed pulse which gets stretched by a dispersive optical setup such as a pair of diffraction gratings.

Chapter 2

Classification of laser beam profiles using machine learning at the ELI-NP high power laser system

The high power laser system at the Extreme Light Infrastructure-Nuclear Physics (ELI-NP) has demonstrated 10 PW power shot capability. It can also deliver beams with powers of 1 PW and 100 TW in several different experimental areas which carry out dedicated sets of experiments. An array of diagnostics is deployed to characterize the laser beam spatial profiles and to monitor their evolution during the amplification stages. Some of the essential near field and far field profiles acquired with CCD cameras are monitored constantly on large screen television for visual observation and for decision making concerning the control and tuning of the laser beams. Here we present results on the beam profiles classification obtained from datasets with over 14,600 near-field and far-field images acquired during two days of laser operation at 1 PW and 100 TW. We utilize supervised and unsupervised machine learning models based on trained neural networks and on an autoencoder. These results constitute an early demonstration of machine learning being used as a tool in the laser system data classification.

Table 2.1: Accuracy of the auto-encoder for different image pre-processing consisting in resizing the image resolution.

Type	Method	Resized Input	Accuracy
Unsupervised	Auto-encoder DNN	250x250	84.9%
Unsupervised	Auto-encoder DNN	100x100	81.2%
Unsupervised	Auto-encoder DNN	75x75	78.0%
Unsupervised	Auto-encoder DNN	50x50	65.0%

2.1 Results and Discussion

2.1.1 Binary classifier performance with ANN

Our ANN for supervised binary classification performed well, separating NF from the FF images. The training was fast, in a few seconds. The input data consisted in two labeled sets FF and NF which included 7236 and 5896 images, respectively, randomly interspersed with noise and multiple-spots beam profiles. A set of 1469 images has been tested following training. The confusion matrix is shown in Fig. 2.1 and shows the number of false predictions. These are given mainly by the noise and multiple-spots images, an example of the classification output being shown in Fig. 2.2.

2.1.2 The DNN and CNN Classifiers Performances

DNN Based on a Custom Autoencoder

The DNN was designed with an auto-encoder optimized for our specific task. We required unsupervised learning to predict 3 classes: ”near-field”, ”far-field”, and ”wedge”. The best accuracy was 84.9% tested with 1,459 images after training the network for about a minute. In this case all images were resized to 250×250 pixels, to maintain consistency throughout training, testing and validation phases. The batch sizes for training were set to 350, and test batch sizes were set to 175. The confusion matrix in Fig. 2.3 shows that most false predictions are linked to the multi-spots images which are predicted both as NF or FF.

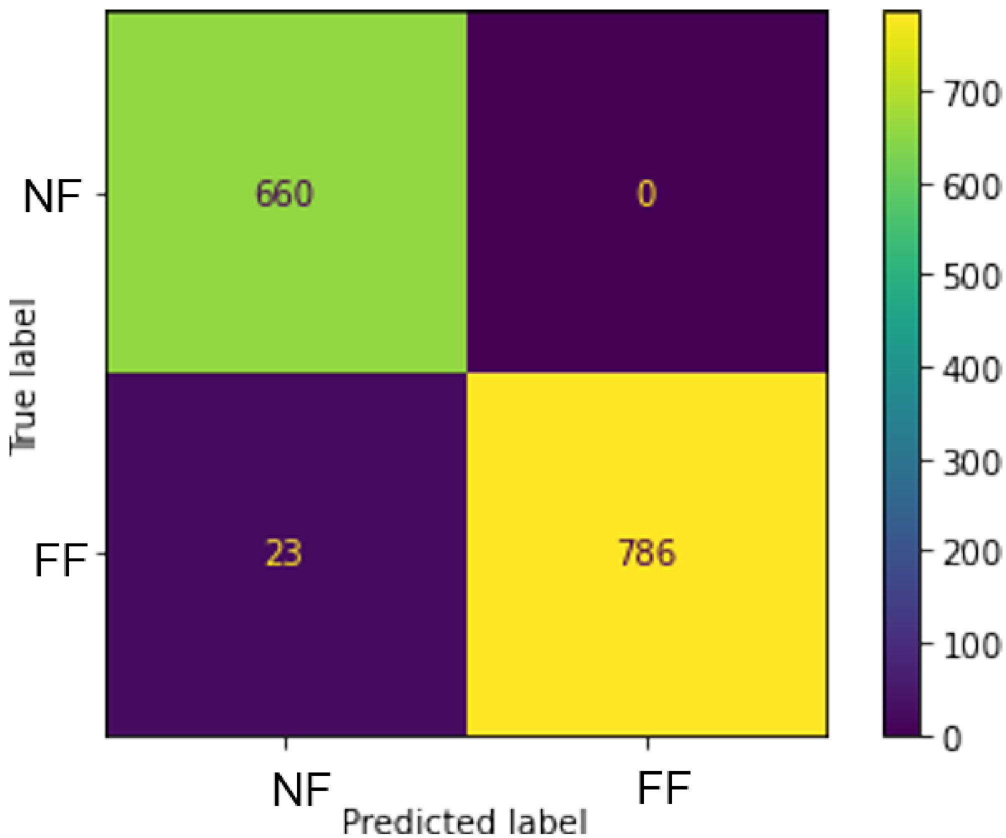

Figure 2.1: Confusion matrix display for binary classification in FF and NF.

2.2 Conclusion

In this work we have implemented different neural network architectures on a common GPU for classification of NF and FF images of laser beam profiles recorded from multiple diagnostic CCD cameras. Included were also inherent "bad images" with noise or no beam profiles and images with multiple beam spots produced during the preparation phase of the laser system which consisted in the alignment of optics. The images were recorded during two days of operation of the high power laser at ELI-NP while delivering beams with powers of 1 PW and 100 TW. The full input dataset consisted in slightly

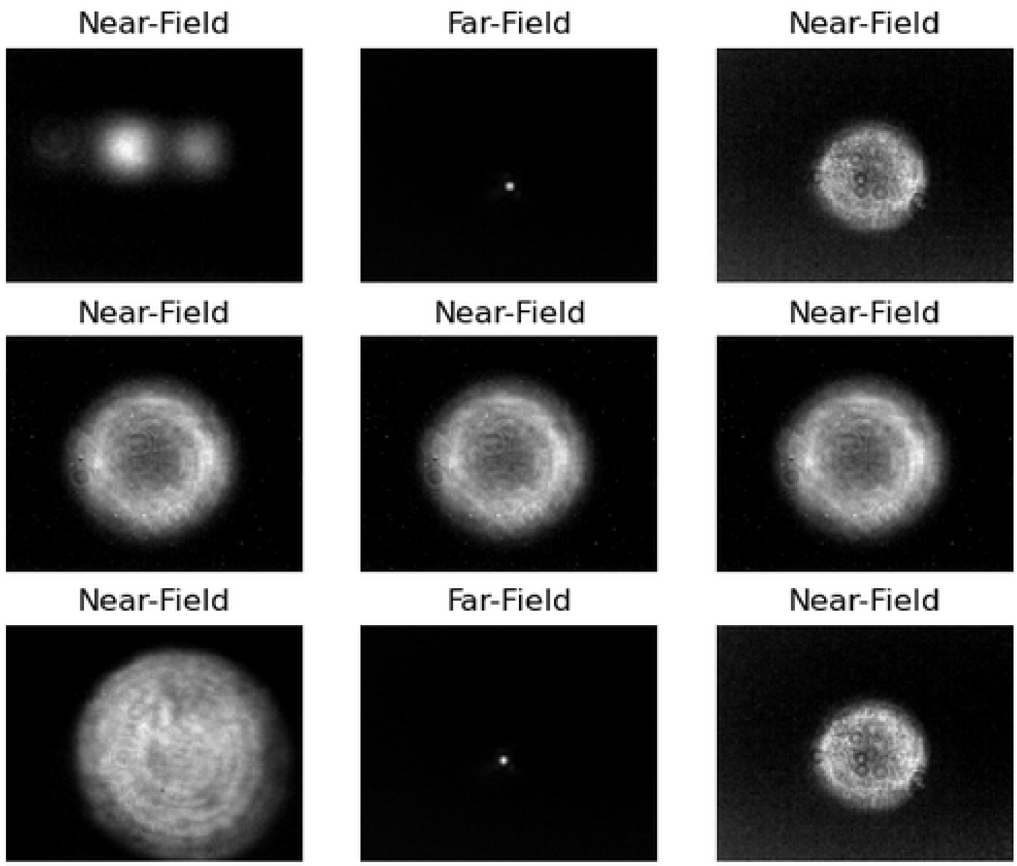

Figure 2.2: Binary classification on an unseen data set. The images are labeled by the ANN output. The multi-spot top (left) image is assimilated as a NF.

over 14600 images.

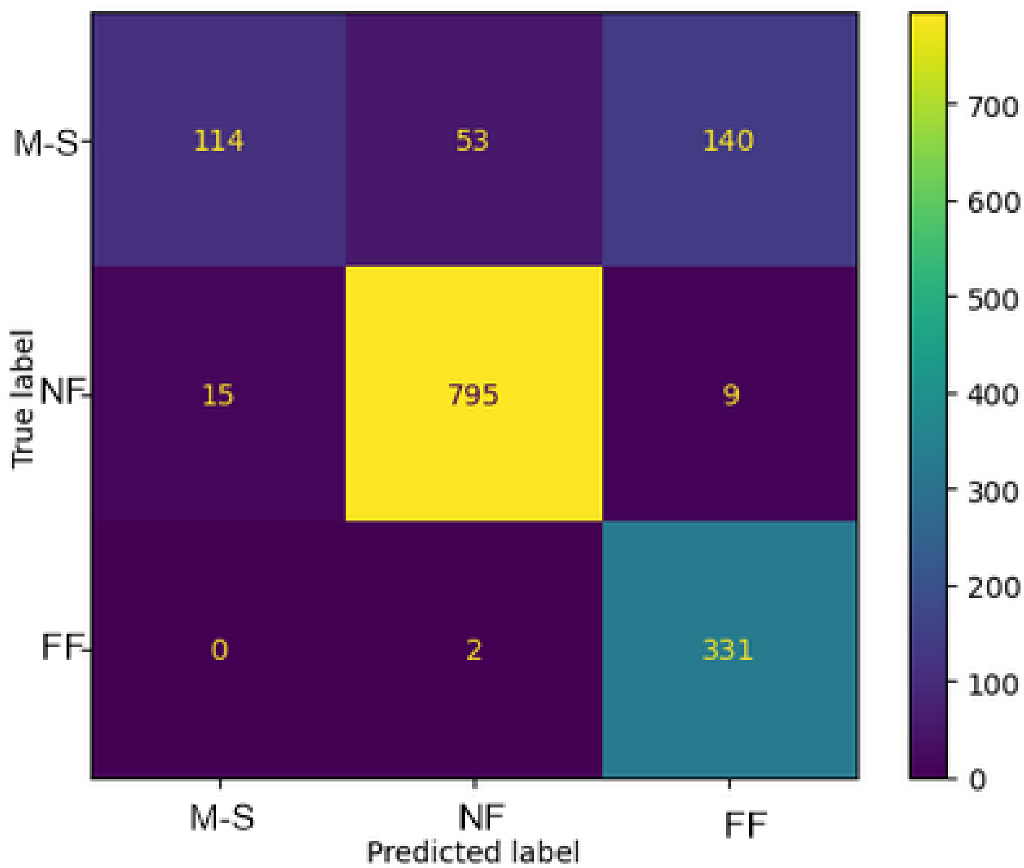

Figure 2.3: Confusion matrix of the autoencoder.

Chapter 3

Real-time Petawatt Laser Beam Profile Classification

We present a hybrid self-supervised model that integrates a convolutional autoencoder (CAE) with a Guassian Mixture Model (GMM) to classify and reconstruct real petawatt laser beam profiles. The model distinguishes between near-field, far-field, and multi-spot beam profiles, demonstrating that self-supervised representations can extract physically meaningful features from unlabeled experimental laser data sets. We achieve 89.4% classification accuracy on our baseline model, improving the previously unsupervised baseline of 85%, under comparable experimental conditions. The integration of a probabilistic layer (GMM) enables more precise clustering of laser beam profiles, achieving 98.9% classification accuracy. Designed for an inference speed up to 1 Hz for live diagnostics on the ELI-NP High Power Laser System (HPLS), our architecture enables real-time state detection. Importantly, we show that high classification performance can emerge even when pixel-level reconstructions are imperfect, indicating that the learned latent representations prioritize physically meaningful structure over image fidelity.

3.1 Introduction

High-Power Laser Systems (HPLSs) are important for advancing the forefront of scientific research in a range of disciplines [4]. For example, petawatt-class lasers have been used to drive relativistic laser-plasma interactions for proton and electron acceleration, enabling compact sources of high-energy particles relevant to nuclear physics and high-field science experiments such as laser-driven ion acceleration and x-ray generation. These experiments depend critically on high beam quality and precise beam alignment, as even slight beam distortions or pointing errors can drastically alter particle acceleration outcomes or the uniformity of generated radiation sources [13]. Maintaining beam quality is therefore essential both to protect expensive optics and to ensure that high-power laser shots produce consistent and interpretable results [7].

3.2 Results

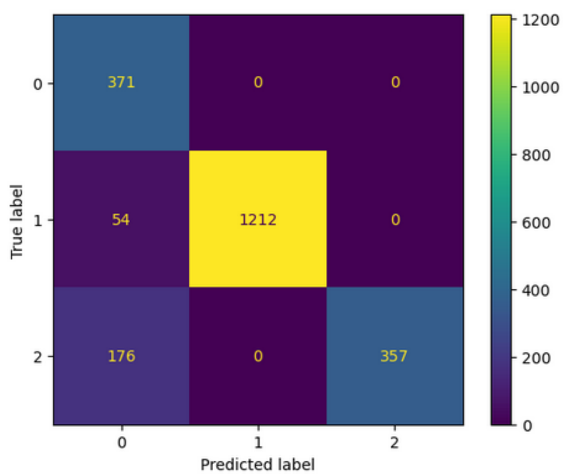

Figure 3.1: Confusion matrix score. In the figure, class 0 represents far-field, class 1 represents near-field, and class 2 represents wedge images.

We trained a convolutional autoencoder using self-supervised representation learning to classify high-power laser beam profiles into three distinct categories: near-field, far-field, and wedge. The model was trained without labels and evaluated on experimental CCD data. The input of the model consists of grayscale images 64×64 obtained from a high-resolution CCD camera, and we have added pre-processing to match the experimental conditions.

During live testing the CCD camera images were found to be in 16 bit format, however, our model was trained on low-resolution 8 bit images. We

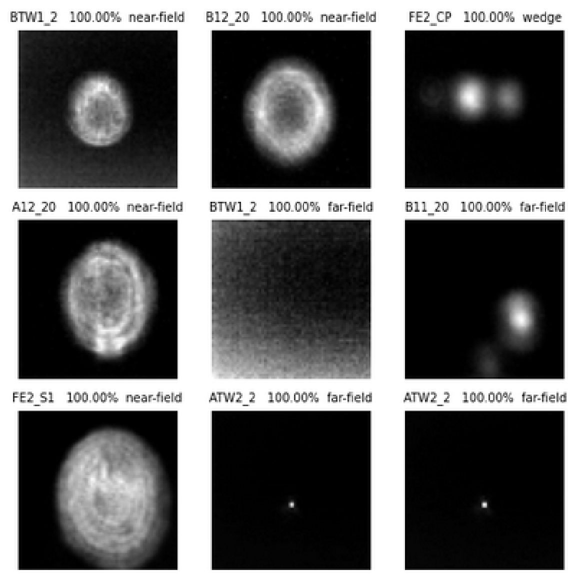

Figure 3.2: Sample of label predictions.

needed to adjust our normalization parameters to successfully account for this change. Near-field and far-field beams were consistently classified correctly with high confidence, which demonstrates that the model learned to selectively discern between features in the latent space without being trained with supervision, as shown in the confusion matrix of Figure 3.1. The near-field and far-field classes are successfully distinguished with high consistency, while wedge beam profiles show partial misclassification as demonstrated in Figure 3.2. This behavior can be attributed to overlapping spatial features and more distinct intra-class variance in wedge profiles, making them much more difficult to discern using the proposed solution presented here.

During non-live testing our model displays both reconstruction outputs and predicted class probabilities. As seen in Figure 3.3, the reconstructed beam profiles maintain blurry yet closely identical spatial intensity distributions of the original experimental images. This consistency validates the model's ability to learn physically meaningful features.

During live acquisition (an example is shown in Figure 3.4), the model's confidence level in each class probability across multiple CCD cameras fluctuated roughly once per second, which reflects beam variation. This behavior indicates that the model is highly sensitive to subtle structural differences in the beam profile, and especially in perceived brightness by the model.

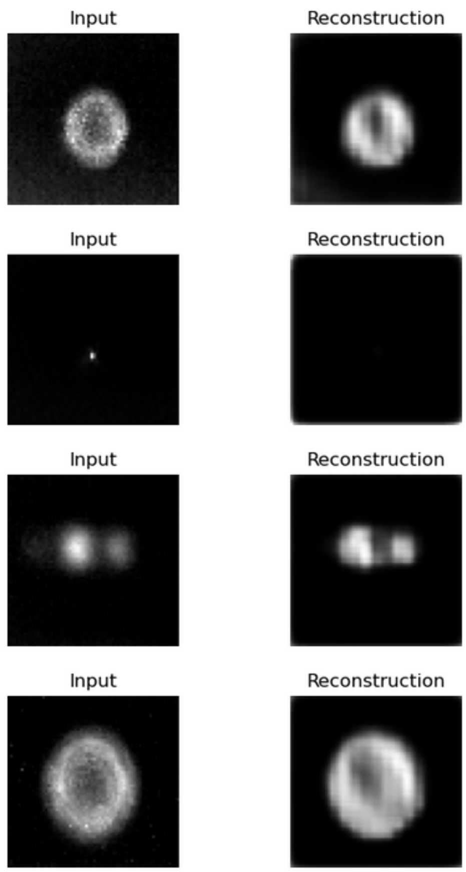

Figure 3.3: Input and reconstructed images.

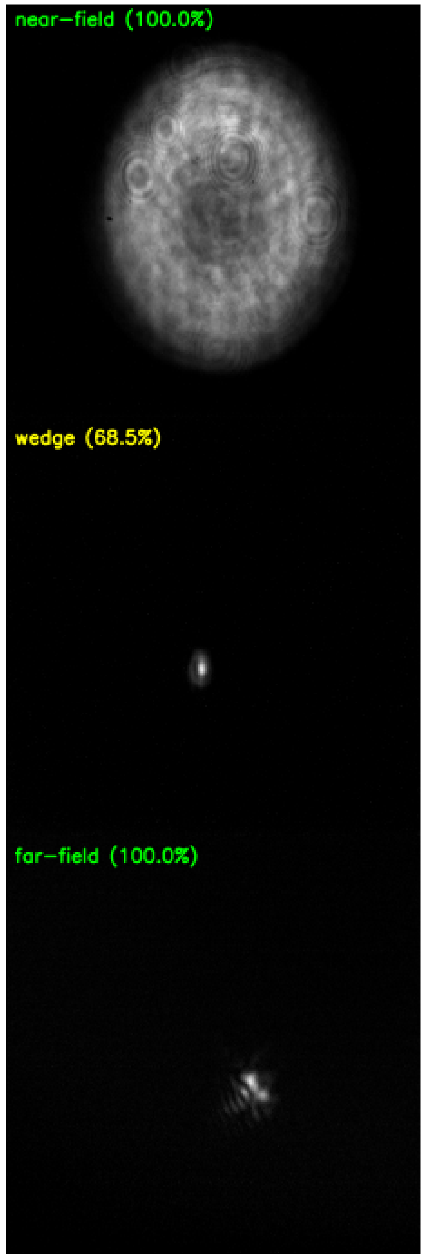

Figure 3.4: Live laser beam profile predictions.

Confidence levels for each beam class varied from 50% to 100% with the classification generally reading above 95% confidence. Wedge profiles consistently exhibited a lower confidence threshold, which highlights the ambiguous nature of this class for the given model.

It is worth noting that varying beam intensity scaling and contrast enhancement significantly influences classification performance. Optimizing exposure normalization is critical for strong model performance on live experimental images, as can be seen by our results received by varying effective brightness and even failing to account for 16 bit to 8 bit numeric differences.

We successfully classified better than 8/9 of our image datasets for near-field, far-field, and wedge (see Figure 3.1). This result includes real noisy data taken from two days of laser beam time utilization. During live testing of our ML model we noticed confident and accurate prediction of near-field and far-field classes, with wedge images being less accurate to classify. The wedge class is likely more ambiguous in the latent space, as there is overlap in the frequency distribution with near-field and far-field beam profiles. Wedge beams often contain asymmetric intensity gradients without sharp intensity discontinuity. Experimental noise, beam jitter, and dynamic clipping further blur class-specific features. As a result, wedge beams do not form a well-separated cluster in image space, making them intrinsically more difficult to classify. Near-field and far-field beams occupy extreme ends of the learned latent space. Wedge beams populate an intermediate region, partially overlapping both classes. The model still achieved strong performance and excellent interpretable predictions across all regimes without supervision.

While the base self-supervised classification achieved 89.4%, the integration of the GMM-based clustering improved the accuracy to 98.90%, as shown in Figure 3.5. This significant gain is attributed to the fact that the model resolves the Wedge class much more precisely due to flexible clustering in the feature space, solving the problem of sometimes being labeled as a Far-field profile. This result provides a suitable threshold for real-time diagnostic support.

3.3 Conclusion

We present a physics-inspired, self-supervised autoencoder for real-time classification and reconstruction of high-power laser beam profiles. Our approach utilizes a multi-objective neural network for high-performance classification

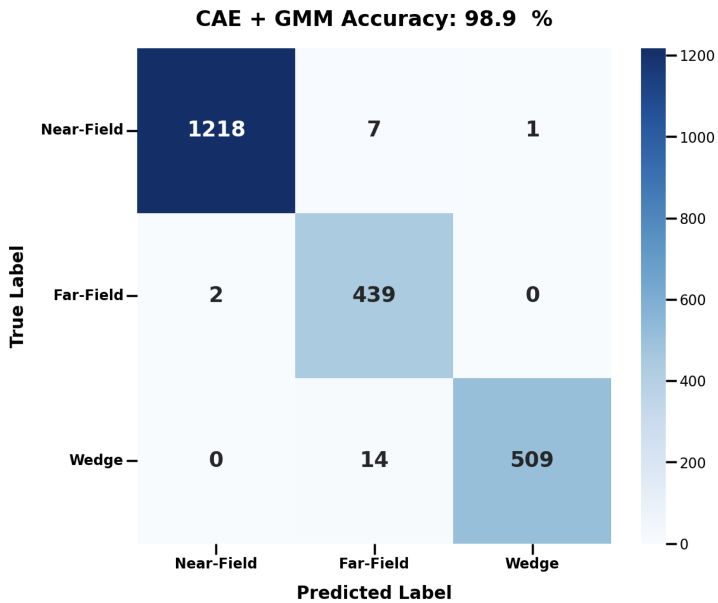

Figure 3.5: Confusion matrix for the hybrid CAE-GMM classifier.

with a confusion matrix score of 89.4%. The integration of a probabilistic layer (GMM) enables more precise clustering of laser beam profiles, achieving 98.9% classification accuracy. This neural network performs both classification and reconstruction of beam profile images. Labels are not used when training this neural network, which makes it robust and generalizable, even to new datasets. New datasets with varying pixel sizes can be classified due to the pre-processing step before real-time classification with cropping and resizing images to align with the training data. This process is aided through the use of physics-inspired loss functions which guide representation learning. These loss functions are more robust against noise from experimental data, and at the same time the model remains sensitive to changes in physical beam state.

Chapter 4

Image Processing in Dusty Plasma Experiments

Strongly coupled dusty plasmas can exhibit turbulent behavior when externally driven by a collimated electron beam with energies in the keV range. The energetic electrons exert a drag force on the negatively charged dust particles, inducing a flow with typical velocities on the order of several millimeters per second. Simultaneously, Coulomb repulsion between particles influences their dynamics, often resulting in irregular and erratic trajectories. The resulting dust flow is captured using a high-speed camera, and Particle Image Velocimetry (PIV) is employed to extract the velocity field. From this, the vorticity distribution is computed to characterize the local rotational features of the flow. In this study, we apply video processing techniques—including contour detection, color-based segmentation, and Principal Component Analysis (PCA)—to analyze turbulent regions within the vorticity maps. These methods enable both qualitative visualization and quantitative assessment of flow structures. The entire implementation is carried out in Python using the OpenCV library.

4.1 Introduction

Strongly coupled dusty plasmas are unique states of matter where charged dust particles, typically micrometer-sized, are suspended in a plasma environment and interact intensely with each other due to their high electric charges [15]. Unlike conventional plasmas, where ions and electrons dominate, the presence of massive dust grains introduces unique dynamics, leading to strong Coulomb coupling that can result in liquid-like or even crystalline behaviors, such as the formation of plasma crystals [3, 11, 16, 5, 6]. These systems bridge plasma physics, condensed matter, and soft matter, offering insights into fundamental processes like self-organization, phase transitions, and wave phenomena. Found in astrophysical settings like planetary rings and comet tails, as well as in laboratory and industrial applications such as semiconductor processing, strongly coupled dusty plasmas are a rich field for studying complex, non-equilibrium systems [9, 2].

4.2 Results and Discussion

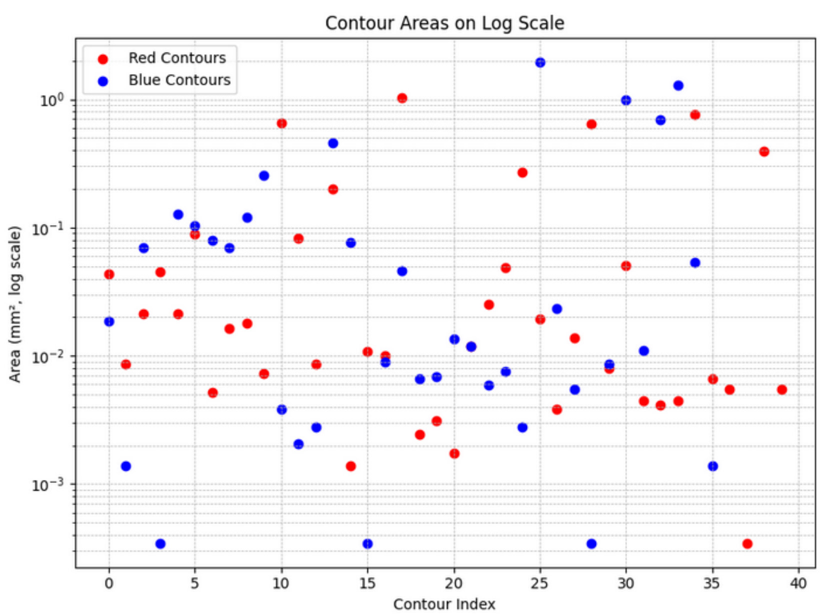

Figure 4.1: Scatter plot of red and blue contour areas.

Using the method described above, we identify 40 red contours (corresponding to regions of positive vorticity) and 36 blue contours (corresponding to negative vorticity) with well-defined areas. A statistical analysis of the vortex contours and their associated areas is presented in Figure 4.1.

The contour index on the x-axis in Figure 4.1 represents the index number of each contour for both red and blue (number 0 for the first contour, 1

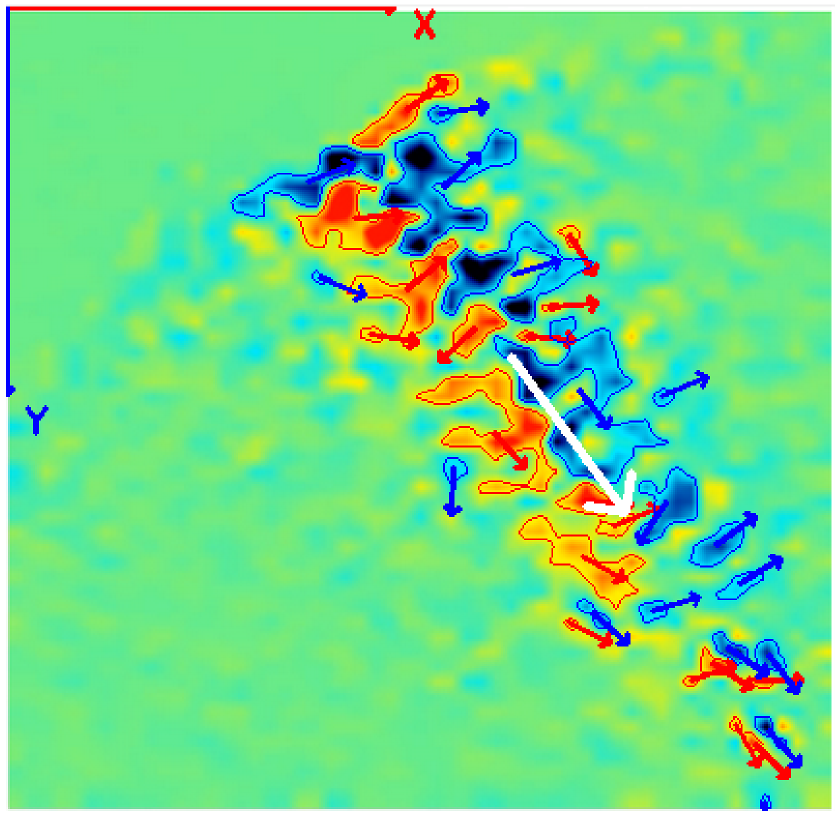

Figure 4.2: PCA vectors drawn over red and blue contours, with white global PCA vector drawn at an angle of 53.5° with OX axis which indicates the general flow direction.

for the 2nd contour, etc). The smallest detected contours have areas of approximately 0.25×10^{-3} mm^2, while the largest reach up to 1 mm^2, spanning nearly three orders of magnitude in area.

In future work, a statistical analysis will be extended to encompass the full set of vorticities acquired at different time instances. The temporal evolution of vortex types (positive or negative) and their sizes will be crucial for characterizing the energy cascade and understanding how energy is transferred from large-scale vortices, driven by the action of the electron beam, to the smallest vortices, where it is ultimately dissipated as heat due to viscosity [14, 8, 1].

The PCA method provides dimensionality reduction, but in our case it allows for the visualization of some specific features in the turbulent dusty

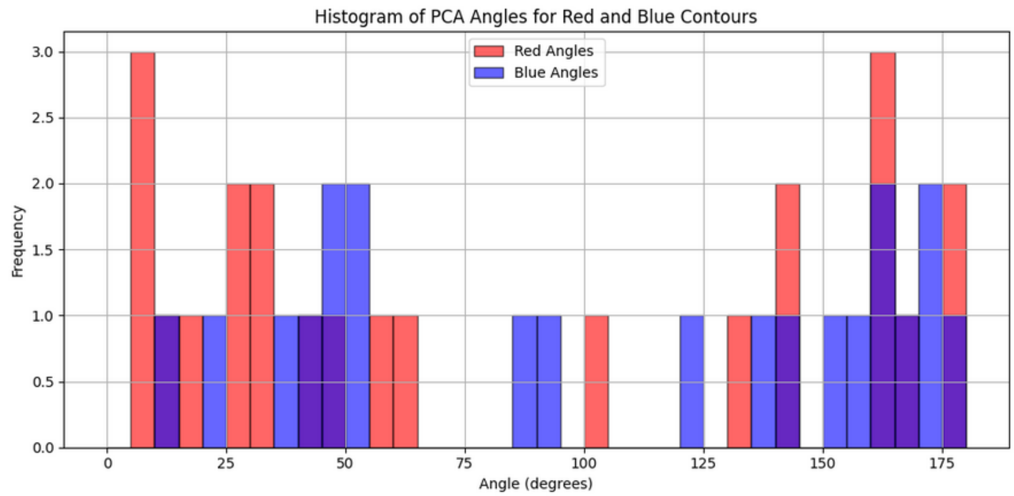

Figure 4.3: Histogram plot of red (with positive vorticity) and blue (with negative vorticity) vector PCA angles.

plasma flow. In Figure 4.2, the PCA vectors represent the elongation of the vortices, which is the direction of maximal variance. Here, PCA vectors represent the general preferred orientation of vortex structures. The PCA histogram shown in Figure 4.3 tells us about the distribution of orientations of the vorticity field throughout the image. The frequency on the y-axis indicates the number of times each contour occurs within the corresponding angle range on the x-axis.

OpenCV uses a pixel-based coordinate system for images. The angles are aligned to the x-axis as a reference where the top left corner of the image is (0,0), moving vertically downward is the positive y-direction (straight down is 90 degrees), and horizontally to the right is the positive x-direction (0 degrees), but angles increase clockwise. In OpenCV's reference: $0° =$ right, $90° =$ down, $180° =$ left, $270° =$ up.

Now, we add OpenCV's context to our histogram, in which angles past $180°$ are normalized to $[0°, 180°)$ to represent principal axes as found by PCA. In our histogram, we have removed the column representing angles $< 5°$ to avoid overlap with $180°$. We notice in our histogram a relatively large number of values between $125°$ and $175°$ that are drawn at those angles in the image; these values are accounted for by the reverse angle by adding $180°$. The global PCA vector (marked in white) is calculated to be at $53.5°$.

This vector represents the dominant direction of the vortex field overall, evidently induced by the e-beam; it is not represented in the histogram as it corresponds to the average of all vectors across the entire image. The broad distribution and apparent randomness of the PCA vectors provide additional evidence for the turbulent character of the dusty plasma flow.

4.3 Conclusion

This study demonstrates the effectiveness of computer vision-based analysis in identifying and characterizing vortex regions within turbulent, strongly coupled dusty plasma flows. High-energy pulsed electron beams with energy of about 13 keV induce complex Coulomb interactions between particles and the beam, driving turbulence in these flows. Our analyses utilize two-dimensional vorticity maps obtained by particle image velocimetry (PIV) that reveal a multitude of positive and negative vorticity regions, visualized in red and blue, respectively. By applying Python functions from the OpenCV library for object segmentation, we accurately delineated vortex contours and quantified their areas. Furthermore, principal component analysis (PCA) was employed to compute vorticity gradients within these regions, with PCA vectors overlaid on contours to illustrate vorticity orientation. A histogram of PCA angles across the image highlights the predominant vorticity orientations, providing insights into the statistical distribution of turbulent vortices. This study is an important step towards analyzing vorticity diffusion and understanding energy transfer scales in turbulent dusty plasmas. Future research will focus on real-time vortex tracking and the development of generative models to produce synthetic datasets, enhancing our ability to predict and model complex plasma dynamics.

Chapter 5

Discussion and Future Directions

This thesis includes advancements in machine learning integration for petawatt-class high-power laser systems. The methodology evolves from an offline use case of supervised learning laser beam profile classification, towards a real-time demonstration of unsupervised learning beam profile classification. This methodological evolution is aimed at future research with the goal of achieving closed-loop control for petawatt lasers. The bulk of the body of work in this thesis is aimed at real-time operational safety, by focusing on spatial beam characterization. Published articles introduce the viability of incorporating machine learning architectures to automate the classification of laser beam profiles in the petawatt regime. The work included in this thesis predominantly enforces these methods to avoid reliance on manual diagnostics. The later work published in 2026 includes contributions to diagnostic monitoring. Not only does this work include automation to reduce manual workload, but it is also trained with physics-informed methods, to achieve learning with tens of thousands of unlabeled images in the dataset.

In addition, the work published in 2025 related to computer vision techniques advances this idea of removing manual measurement techniques. The paper includes a methodology designed to study and characterize the behavior of turbulent strongly coupled dusty plasmas. The research presented in this work utilizes advanced image processing techniques and computer vision methods to extract quantitative results from particle image velocimetry data.

The work in this thesis is aimed at merging the domains of high-power laser physics, with cutting edge data-driven computational methods. A modern approach to continue in this manner would be to include an AI agent capable of closed-loop communication and control of the HPLS. Such an extension could include closed-loop agents capable of dynamically adjusting deformable mirrors and position optical stages to prevent damage from occurring on valuable equipment such as the pulse compressors.

Bibliography

[1] A. P. Almoguera and D. Kivotides. Vortex dynamics of turbulent energy cascades. *Phys. Fluids*, 36(12):125156, 2024.

[2] J. Beckers, J. Berndt, D. Block, M. Bonitz, P. J. Bruggeman, et al. Physics and applications of dusty plasmas: The perspectives 2023. *Physics of Plasmas*, 30:120601, 2023.

[3] J. H. Chu and Lin I. Direct observation of coulomb crystals and liquids in strongly coupled rf dusty plasmas. *Physical Review Letters*, 72:4009, 1994.

[4] C. N. Danson, C. Haefner, J. Bromage, et al. Petawatt and exawatt class lasers worldwide. *High Power Laser Science and Engineering*, 7:e54, 2019.

[5] M. G. Hariprasad, P. Bandyopadhyay, G. Arora, and A. Sen. Experimental observation of a dusty plasma crystal in the cathode sheath of a dc glow discharge plasma. *Physics of Plasmas*, 25(12):123704, 2018.

[6] S. Jaiswal, C. Belt, A. Kananovich, and E. M. Aguirre. Structural transformation of dusty plasma crystal in dc discharge plasma by changing confinement ring bias. *Physical Review Research*, 6:013119, 2024.

[7] A. Jeandet, A. Borot, K. Nakamura, et al. Spatio-temporal structure of a petawatt femtosecond laser beam. *Journal of Physics: Photonics*, 1(3):035001, 2019.

[8] R. P. J. Kunnen, H. J. H. Clercx, and B. J. Geurts. Vortex statistics in turbulent rotating convection. *Physical Review E*, 82:036306, 2010.

[9] R. L. Merlino and J. A. Goree. Dusty plasmas in the laboratory, industry, and space. *Physics Today*, 57(7):32–38, 2004.

[10] Tom M. Mitchell. *Machine Learning*. McGraw-Hill, 1997.

[11] G. E. Morfill, B. M. Annaratone, P. Bryant, A. V. Ivlev, H. M. Thomas, M. Zuzic, and V. E. Fortov. A review of liquid and crystalline plasmas—new physical states of matter? *Plasma Physics and Controlled Fusion*, 44:B263, 2002.

[12] Francisco A. Rodrigues. Machine learning in physics: a short guide. *Europhysics Letters*, 144(2):22001, 2023.

[13] M. Schollmeier, K. Harres, F. Nürnberg, et al. Laser beam-profile impression and target thickness impact on laser-accelerated protons. *Physics of Plasmas*, 15(5):053101, 2008.

[14] S. Sharma, R. Wani, P. Srivastav, M. Sharma, S. Bose, Y. Saxena, and S. Tiwari. Observation of kolmogorov turbulence due to multiscale vortices in dusty plasma experiments. *Physics of Plasmas*, 31(12):123704, 2024.

[15] P. K. Shukla and B. Eliasson. Colloquium: Fundamentals of dust-plasma interactions. *Reviews of Modern Physics*, 81:25, 2009.

[16] M. H. Thoma, M. Kretschmer, H. Rothermel, H. M. Thomas, and G. E. Morfill. The plasma crystal. *American Journal of Physics*, 73(5):420–424, 2005.